

Enhancing stability and magnetism of ThMn₁₂-type cerium-iron intermetallics by site substitution

Churna Bhandari ^{1,*} and Durga Paudyal ^{1,2}

¹*Critical Materials Institute, Ames Laboratory, U.S. Department of Energy, Iowa State University, Ames, Iowa 50011, USA*

²*Department of Electrical and Computer Engineering, Iowa State University, Ames, Iowa 50011, USA*



(Received 18 November 2021; accepted 21 March 2022; published 5 April 2022)

There is considerable research interest in discovering new permanent magnetic materials that perform equally as champion neomagnets, with the minimal use of critical rare-earth elements. Recently ThMn₁₂-type (1:12) rare-earth iron (Ce-Fe) intermetallic materials have been on the frontline of research as Ce is naturally abundant that drastically lowers the cost of permanent magnets. Here, we investigate the lattice stability and electronic and magnetic properties of Ti- or Zr-substituted CeFe₁₂ and CeFe₁₂N using density functional theory. We find negative formation energy for all compositions in the bulk structure with respect to unaries except for CeFe₁₂. The inclusion of nitrogen in the interstitial sites of CeFe₁₂ improves its chemical stability by reducing the formation energy. The first time successfully calculated phonon frequencies including 4*f* electrons indicate that all compositions are dynamically stable. With the help of electronic structure calculations, we demonstrate that cerium exhibits the mixed-valence character in 1:12 materials. The mixed-valency sensibly affects the magnetocrystalline anisotropy (MCA) and magnetic moment. Nitrogen improves the net magnetic moment by influencing the spin polarization with extra electrons, although it has the opposite effect in the MCA constant, K_1 . The predicted value of K_1 confirms all compounds uniaxial along the crystalline *c* axis. Especially for CeZrFe₁₁, K_1 is the largest in which Ce exhibits Ce³⁺ ($S = 1/2$), and Ce(4*f*) spin-density contour is elongated towards the uniaxial direction. The substantially large values of the MCA and magnetic moments suggest that these critical element-free materials qualify for high-performance permanent magnets.

DOI: [10.1103/PhysRevResearch.4.023012](https://doi.org/10.1103/PhysRevResearch.4.023012)

I. INTRODUCTION

Iron-rich ThMn₁₂-type (1:12) rare-earth (R) intermetallics (RFe₁₂) are potential candidate materials for permanent magnets with a large magnetocrystalline anisotropy (MCA) that stems from the interplay between strong spin-orbit coupling (SOC) and crystal field effect in R-4*f* states, and a large magnetization from the 3*d* transition metal elements [1–7]. Still, the existing challenge is to predict a high-performance 1:12 permanent magnetic material as par with champion neomagnet [8], that is cost-effective and stable at operating temperatures. Especially the cerium-based 1:12 materials have been attractive because cerium is naturally abundant that could drastically reduce the cost of permanent magnets. In addition, rare earth and iron 1:12 phases can be stabilized experimentally by the elemental substitutions and/or the addition of extra elements in the interstitial sites [5–7,9,10]. For example, CeTi_{*x*}Fe_{12–*x*} has been successfully synthesized by substituting iron (Fe) with titanium (Ti) [11–13]. Analogously one could synthesize the isovalent Zr-substituted compositions with improved magnetic anisotropy. The in-

terstitial *p*-block elements such as nitrogens as well as the substituted elements help in tuning the valence state of cerium [11,14,15] including the intrinsic magnetic properties such as MCA, magnetization, and Curie temperature of CeTi_{*x*}Fe_{12–*x*} [16]. More importantly, their phonon-driven stability is yet to be examined.

The crystal structure of ThMn₁₂-type compound is tetragonal with space group I4/mmm (139) in which rare-earth element substitutes thorium (Th) at 2*a*, and Fe atoms substitute three nonequivalent Mn atoms in 8*i*, 8*j*, and 8*f* Wyckoff positions. While there are three nonequivalent Fe sites in the 1:12 composition, Ti has a very strong 8*i* or 8*j* Fe-site preference depending upon the choice of Ce in 2*a* or 2*b* site [12,13]. The substituted rare-earth ($R = \text{Sm}$ and Nd) based 1:12 compounds show very intriguing magnetic properties such as the change in the sign of the second-order crystal field parameter (A_{20}) due to the different number of 4*f* electrons [8,12,13,17,18]. The Ce based-compounds are even more subtle because of localization and/or delocalization tendency of 4*f* electrons [19,20] dependent on the crystal environment. By fine-tuning of 4*f*-electronic states could help to control the intrinsic permanent magnetic properties.

While a few theoretical studies [21–24] have been performed in Ti-substituted Ce-based-compositions (CeTiFe₁₁ and CeTiFe₁₁N), they disagree in the MCA results. Authors in Reference [24] report an increase in MCA constant K_1 in CeTiFe₁₁N using a model calculation, at low temperature, while experiments show the opposite [12,16]. On the other hand, the tight-binding atomic sphere approximation (ASA)

*cbb@ameslab.gov

Published by the American Physical Society under the terms of the [Creative Commons Attribution 4.0 International license](https://creativecommons.org/licenses/by/4.0/). Further distribution of this work must maintain attribution to the author(s) and the published article's title, journal citation, and DOI.

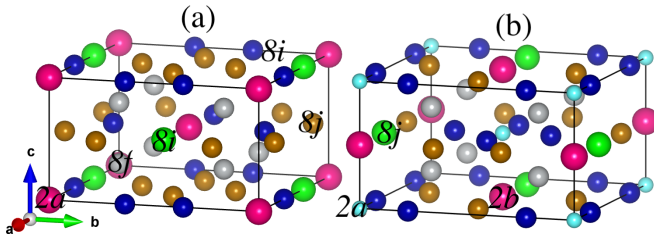


FIG. 1. Crystal structures with the same crystallographic axes ($2a$ site as the origin of both unit cells) of (a) CeTiFe_{11} and (b) $\text{CeTiFe}_{11}\text{N}$. The nonequivalent Fe atoms are purple, blue, and brown balls, which are labeled by their Wyckoff-site symbols $8j$, $8i$, and $8f$. Ce is red located at $2a$ in CeTiFe_{11} and $2b$ in $\text{CeTiFe}_{11}\text{N}$. Ti is green at $8i$ in CeTiFe_{11} and $8j$ in $\text{CeTiFe}_{11}\text{N}$. The cyan ball is N at $2a$.

calculations produced the opposite results in Ref. [22]. The assumption $J = 5/2$ state for Ce with $S = 1/2$ and $L = 3$ in the model is not necessarily true for real Ce-based 1:12 compounds as indicated by our density functional theory (DFT) calculations that yield the mixed-valency of Ce in contrast to the previous DFT calculations [21] where it was assumed to be Ce^{3+} . Indeed, x-ray absorption fine structure (XAFS) measurement demonstrates that Ce exhibits an intermediate valence character in CeTiFe_{11} [11], which is also discussed in Ref. [6]. This valence fluctuation of Ce between Ce^{3+} (magnetic) and Ce^{4+} (nonmagnetic) is very critical for Ce-based compounds because it affects the magnitudes of MCA and the net magnetic moment [19]. For instance, Ce^{3+} would lead to a stronger MCA as compared to Ce^{4+} . Moreover, to the best of our knowledge, the dynamical stability, which is a bottleneck for the success of Ce-based 1:12 materials in permanent magnet applications, has not been studied in the literature.

Using DFT, we study stability (in terms of formation energy and phonon dynamics) and electronic and magnetic properties of CeFe_{12} and its known Ti- and potential Zr-substituted compositions, including the interstitial nitrogens. Following are the key results. (i) All substituted compounds are chemically stable as indicated by the calculated negative formation energies. (ii) None of these compositions have soft-mode (imaginary) phonon frequencies, which indicate all of them are dynamically stable. (iii) The added nitrogen improves the chemical stability of both Ti- and Zr-substituted compositions as well as the net magnetic moments. (iv) The calculations confirm all of them are uniaxial along the c axis, especially for CeZrFe_{11} , the MCA constant, K_1 , is the largest. (v) Nitrogen leads to a reduction of K_1 in all compounds, which is the opposite to that seen in Nd-based counterparts [8].

II. COMPUTATIONAL DETAILS

We performed DFT calculations with Vienna *ab initio* simulation package (VASP) [25] in projected augmented wave (PAW) method [26] using Perdew-Burke-Ernzerhof (PBE) generalized gradient approximation (GGA) exchange-correlation functional [27,28]. Full structural optimizations were carried out treating $\text{Ce}(4f)$ as (i) frozen core states with GGA and (ii) valence states with and without on-site elec-

tron correlation within Dudarev's approximation $U_{\text{eff}} = U - J$ [29]. To obtain the magnetocrystalline anisotropy energy (MAE), full relativistic spin-orbit coupling self-consistent charge density calculations were carried out including the $\text{Ce}(4f)$ electrons. The physical properties of light rare earth, Ce (with $U_{\text{eff}} = 4.5$ eV), are not so sensitive for the choice of U in the range of 4–7 eV [30]. We used total energy cutoff of 600 eV and \mathbf{k} -mesh of $4 \times 4 \times 7$ for the full Brillouin-zone integration. Further, we checked the \mathbf{k} -point convergence of MAE by increasing \mathbf{k} -mesh up to $8 \times 8 \times 14$, however no significant difference was found in the results. Phonon frequencies were computed with *frozen phonon* (adiabatic) approximation [31,32].

III. RESULTS AND DISCUSSION

A. Structure details

1. Site preference

The crystal structures of CeTiFe_{11} and $\text{CeTiFe}_{11}\text{N}$ are shown in Fig. 1. The Wyckoff's position of each atom is shown in Fig. 1 where one Ti replaces one Fe($8i$) in CeTiFe_{11} and one Fe($8j$) in $\text{CeTiFe}_{11}\text{N}$. We note that Fe($8i/8j$) positions are interchangeable with respect to the octahedral sites of Ce/N ($2b/2a$) [12]. To demonstrate the site preference, we compute the total energy in the fully relaxed structure after substituting Ti or Zr in different Fe sites. In our calculations, we use $\text{Ce}(4f)$ states as valence-states and the on-site electron correlation to screen the total energies in different site substitutions. The total energies per unit cell (u.c.) of the substituted compound at various sites are given in Table I. The results show the site preference order $8i > 8j > 8f$ in which $8i$ has the lowest energy consistent with the experiment for CeTiFe_{11} [13]. The same situation is found for Zr, while energy at $8f$ is lower than at $8j$. Zr is a very peculiar element that tends to partially replace the rare-earth element such as Sm in Sm-based 1:12 compounds [35,36]. To check whether this is also true for Ce composition, we compute the formation energy relative to elements by substituting 50% Ce with Zr ($\text{Ce}_{0.5}\text{Zr}_{0.5}\text{Fe}_{12}$). The formation energy of $\text{Ce}_{0.5}\text{Zr}_{0.5}\text{Fe}_{12}$ is larger by a factor of 3 than that of CeZrFe_{11} (Table III). Therefore it is unlikely that Zr goes to the Ce site. With the addition of nitrogens, for both $\text{CeTiFe}_{11}\text{N}$ and $\text{CeZrFe}_{11}\text{N}$, the total energies are the lowest at the $8j$ site, which agrees with the experiment for $\text{CeTiFe}_{11}\text{N}$ [12].

2. Optimized structure

To understand the effect of $\text{Ce}(4f)$ electrons and their on-site electron correlation in structural parameters, we optimize the structure in three different schemes. For this, we also consider a hypothetical CeFe_{12} and CeFe_{12}N . The volume of CeFe_{12} is overestimated by $\sim 2.6\%$ in GGA with $4f$ -core electrons. While the GGA + U corrects the overestimate, it yields slightly larger than the value without U . As expected, the CeFe_{12} volume expands by $\sim 2.7\%$ with the addition of nitrogens in all calculations. Surprisingly, GGA (with $4f$ -core electrons) shows the opposite trend (an underestimate) for CeFe_{12}N . Overall, both GGA and GGA + U with $4f$ -valence electrons predict similar lattice parameters.

TABLE I. Total energy per formula unit (in eV) computed with GGA + U method. The total energy for Ti/Zr in $8i$ site is taken as zero reference for the comparison. The substituted element prefers Fe($8i$) site in CeFe₁₂ and Fe($8j$) site in CeFe₁₂N.

E	CeTiFe ₁₁ N	CeTiFe ₁₁	CeZrFe ₁₁ N	CeZrFe ₁₁
Ti/Zr($8i$)	0	0	0	0
Ti/Zr($8j$)	-0.30	0.34	-0.81	1.62
Ti/Zr($8f$)	0.40	0.71	0.41	0.87

Next, we discuss the structures of Ti/Zr-substituted compositions. The substituted element is randomly distributed in its favorable Fe site that lowers the tetragonal symmetry resulting in a small mismatch between calculated in-plane lattice constants. We present the only average value for in-plane lattice constant (Table II). The CeFe₁₂ volume increases by ~3% (in GGA with $4f$ core) with Ti substitution, which is likely due to the slightly larger atomic size of Ti. As expected, with nitrogen, the volume further expands in all cases. The volume is overestimated for all compositions (without nitrogen) with $4f$ -core approximation as seen in CeFe₁₂. On the other hand, for the nitrogenated compositions, volumes are underestimated as in CeFe₁₂N.

Surprisingly, the calculated volumes are slightly underestimated for experimentally known Ti compositions despite the well-known GGA functional, which generally overestimates. It is probably due to the thermal expansion of lattice constants because experiments are performed at room temperature. A similar underestimate of the lattice parameters is also reported in previous DFT calculations [15,33,34,34] for Ce, Fe, and Ti metals and the related compounds. Overall, including $4f$ -valence electrons, the optimized structures of CeTiFe₁₁ and CeTiFe₁₁N are found in better agreement with the experiments [13,16].

B. Formation energy

We compute the formation energies for CeFe₁₂N _{x} and CeAFe₁₁N _{x} ($A = \text{Ti, Zr}$ and $x = 0, 1$) compounds. The forma-

tion energies for CeFe₁₂N _{x} ($x = 0, 1$) with respect to unaries Ce, Fe, Ti, and N are obtained using the expression

$$E_f(\text{CeFe}_{12}\text{N}_x) = E(\text{CeFe}_{12}\text{N}_x) - E(\text{Ce}) - 12E(\text{Fe}) - xE(\text{N}), \quad (1)$$

where $E(\text{CeFe}_{12}\text{N}_x)$, $E(\text{Ce})$, $E(\text{Fe})$, and $E(\text{N})$ are total energies of CeFe₁₂ (per f.u.), and Ce, Fe, and N (per atom) in the crystalline form. The formation energy for CeAFe₁₁N _{x} ($A = \text{Ti, Zr}$ and $x = 0, 1$) is calculated as

$$E_f(\text{CeAFe}_{11}\text{N}_x) = E(\text{CeAFe}_{11}\text{N}_x) - E(\text{Ce}) - E(A) - 11E(\text{Fe}) - xE(\text{N}), \quad (2)$$

where $E(A)$ and $E(\text{CeAFe}_{11}\text{N}_x)$ are the total energies of A and CeAFe₁₁N _{x} .

The formation energies of all compositions calculated relative to unaries, as given in Table III, are all negative except for CeFe₁₂. The positive formation energy is the reason why CeFe₁₂ cannot be synthesized experimentally in the bulk form. An improvement in the formation energy for CeTiFe₁₁ is due to a larger overlap between Ce and Ti valence orbitals as indicated by electronic structure (discussed below), despite a slight mismatch between atomic sphere sizes of Fe and Ti. Next, we compute its formation energy relative to binary FeTi and CeFe₁₂ as

$$E_f(\text{Ce}_2\text{Ti}_2\text{Fe}_{22}) = E(\text{Ce}_2\text{Ti}_2\text{Fe}_{22}) - 2E(\text{CeFe}_{12}) - E(\text{FeTi}) + 4E(\text{Fe}), \quad (3)$$

 TABLE II. Optimized lattice constants and comparison with available experimental data in different schemes. We show only the average value for a and b lattice constants in the site-substituted compositions as they differ slightly due to low symmetry.

Method	CeFe ₁₂		CeFe ₁₂ N		CeTiFe ₁₁ N		CeTiFe ₁₁		CeZrFe ₁₁ N		CeZrFe ₁₁	
	a	c	a	c	a	c	a	c	a	c	a	c
This work ^a	8.59	4.66	8.35	4.81	8.49	4.84	8.61	4.70	8.65	4.87	8.68	4.79
This work ^b	8.50	4.64	8.51	4.80	8.57	4.80	8.52	4.68	8.65	4.87	8.51	4.85
This work ^c	8.56	4.64	8.51	4.81	8.58	4.83	8.53	4.68	8.67	4.89	8.53	4.84
Expt.	-	-	-	-	8.57	4.87 ^d	8.53	4.78 ^e	-	-	-	-
	-	-	-	-	-	-	8.54	4.78 ^d	-	-	-	-
	-	-	-	-	-	-	8.53	4.81 ^f	-	-	-	-
Theory	8.57	4.66 ^g	-	-	-	-	8.52	4.68 ^h	-	-	-	-

^aGGA with $4f$ electrons as core.

^bGGA with $4f$ electrons as valence.

^cGGA + U with $4f$ electrons as valence.

^dReference [4].

^eReference [16].

^fReference [13].

^gGGA no $4f$ electrons for Ce with energy cutoff 400 eV in Ref. [33].

^hGGA with $4f$ electrons for Ce in Ref. [34].

TABLE III. Calculated formation energy (E_f) in eV per f.u. with GGA. The values are all negative except for CeFe₁₂(1 : 12) suggesting that later is unstable at 0 K.

series	CeFe ₁₂	CeFe ₁₂ N	CeTiFe ₁₁ N	CeTiFe ₁₁	CeZrFe ₁₁ N	CeZrFe ₁₁
E_f (eV)	0.14	-1.34	-2.37	-0.93	-1.68	-0.35

where $E(\text{CeFe}_{12})$ and $E(\text{FeTi})$ are energies of CeFe₁₂ and FeTi. The formation energy obtained relative to the binary is still negative. We also compute its formation energy with respect to CeFe₂ (1:2), CeFe₁₂, and FeTi, which is slightly higher than that computed with respect to Ce₂Fe₁₇ (2:17) and FeTi. The formation energy calculated with respect to stable CeFe₂ and FeTi [$E_f = E(\text{Ce}_2\text{Ti}_2\text{Fe}_{22}) - 2E(\text{CeFe}_2) - 2E(\text{FeTi}) - 16E(\text{Fe}) > 0$] is positive. This indicates that CeFe₂ and FeTi are the potential competing phases with CeTiFe₁₁. A more detailed description of the temperature-dependent phase stability of these compounds is available in Ref. [34], which indicates that CeFe₁₁Ti is stable at high temperature, while the 1:2 and 2:17 phases are stable at lower temperatures. Next, we examine the formation energy of CeZrFe₁₁ relative to other possible phases, e.g., ZrFe, ZrFe₂, and CeFe₁₂ as

$$E_f(\text{Ce}_2\text{Zr}_2\text{Fe}_{22}) = E(\text{Ce}_2\text{Zr}_2\text{Fe}_{22}) - 2E(\text{CeFe}_{12}) - E(\text{ZrFe}_2) - E(\text{ZrFe}) + 5E(\text{Fe}), \quad (4)$$

where $E(\text{ZrFe})$ and $E(\text{ZrFe}_2)$ are energies of ZrFe and ZrFe₂. The formation energy of CeZrFe₁₁ is positive which suggests that CeZrFe₁₁ competes with ZrFe and ZrFe₂.

The inclusion of nitrogens leads to the negative formation energy for CeFe₁₂, although the bulk CeFe₁₂N has not been reported experimentally. The formation energies also decrease in Ti/Zr-substituted compositions with the addition of nitrogens because of significant overlap of N(2*p*) with Ce(4*f*), Fe(3*d*), and Ti(3*d*) or Zr(4*d*) orbitals [PDOS Fig. 5] around the Fermi level as seen in CeFe₁₂N. The difference in the formation energies of Ti/Zr-substituted compositions is likely due to their different atomic sizes.

C. Dynamical stability

Phonon frequencies help in understanding the dynamical stability of materials. Recently, phonon calculations are reported for CeFe₁₂ in Ref. [33] by neglecting the Ce(4*f*) states. Here, we investigate the phonon frequencies and the phonon density of states of these materials treating the 4*f* electrons as valence electrons. In addition, for the first time, we report the phonon frequencies of Ti/Zr-substituted compositions and their nitride counterparts.

To find accurate phonon frequencies atomic positions are optimized with a tight force convergence threshold ($< 10^{-4}$ Å/atom) in the primitive cell. For the force calculations, we use the converged $4 \times 4 \times 4$ **k** mesh in proportion to the dimensions of a supercell in Brillouin zone sampling. The phonon frequencies and density of states are computed by diagonalizing the dynamical matrices generated with the finite displacement method using the *phonopy* program [37]. The

dynamical matrix is given by

$$D_{\alpha\beta}(\mathbf{q}, jk) = \frac{1}{\sqrt{M_j M_k}} \sum \Phi_{\alpha\beta}(\tau_{\mathbf{a}}, jk) e^{i\mathbf{q} \cdot \tau_{\mathbf{a}}}, \quad (5)$$

where i and j label atoms, α and β are axis indices, M is atomic mass, $\tau_{\mathbf{a}}$ is the displacement from the equilibrium, and $\Phi_{\alpha\beta}(\tau_{\mathbf{a}}, jk)$ is a second rank tensor (second derivative of energy with respect to the displacement).

First, we discuss the phonon band structure of CeFe₁₂ as shown in Fig. 2. The phonon dispersions show no-soft modes (imaginary frequencies) that confirm CeFe₁₂ dynamically stable. However, as discussed above, it does not form in bulk because of the positive formation energy. We also compute atom-projected phonon density of states (PhDOS) [Fig. 2(b)]. Here, we show only the average PhDOS for Fe atoms, although it differs slightly due to their different lattice sites. The figure shows a small vibrational hybridization between Ce and Fe atoms around 10–30 meV, as expected, due to the difference in their atomic masses. The phonons in the low energy sector are primarily cerium-derived since it has a larger mass.

Similar phonon frequencies are obtained for CeFe₁₂N, except now we have extra high-lying optic modes around 50–80 meV [Fig. 2(c)]. As expected for light elements, these high energy modes are mainly N-derived vibrational modes with some hybridization with Ce and Fe as shown in Fig. 2(d).

Next, we discuss the phonons in Ti/Zr-substituted compositions (Fig. 3). In this case, because of the random Fe-site occupancies of Ti/Zr, the tetragonal symmetry is broken, which leads to various nonequivalent Fe-sites. We only present the average PhDOS for Fe. Ti and Fe have very similar vibrational hybridization with Ce, as expected as their atomic masses are similar. On the other hand, Zr has relatively higher vibrational hybridization with Ce because of its larger atomic mass. In both Ti/Zr-substituted compositions, we find no imaginary or soft-mode phonon frequencies, which confirms them dynamically stable. In addition, these compositions with added nitrogens (CeTiFe₁₂N/CeZrFe₁₂N) are also dynamically stable (Fig. 3) with extra N-like higher energy optic modes as seen in CeFe₁₂N.

To see the effect of Ti substitution or nitrogens in the thermodynamic potential, we compute the vibrational Helmholtz free energy as a function of temperature T , which reads

$$F_{\text{vib}}(T) = \frac{1}{N_q} \sum_{\mathbf{q}\nu} \left\{ \frac{\hbar\omega_{\mathbf{q}\nu}}{2} + k_B T \ln \left[1 - \exp\left(-\frac{\hbar\omega_{\mathbf{q}\nu}}{k_B T}\right) \right] \right\}, \quad (6)$$

where N_q is number of **q** points in the full Brillouin zone, $\hbar\omega_{\mathbf{q}\nu}$ is phonon frequency, and \hbar is Planck's constant. Figure 4 shows the variation of vibrational Helmholtz free energy (F_{vib}) as a function of temperature T . We find an upward shift of

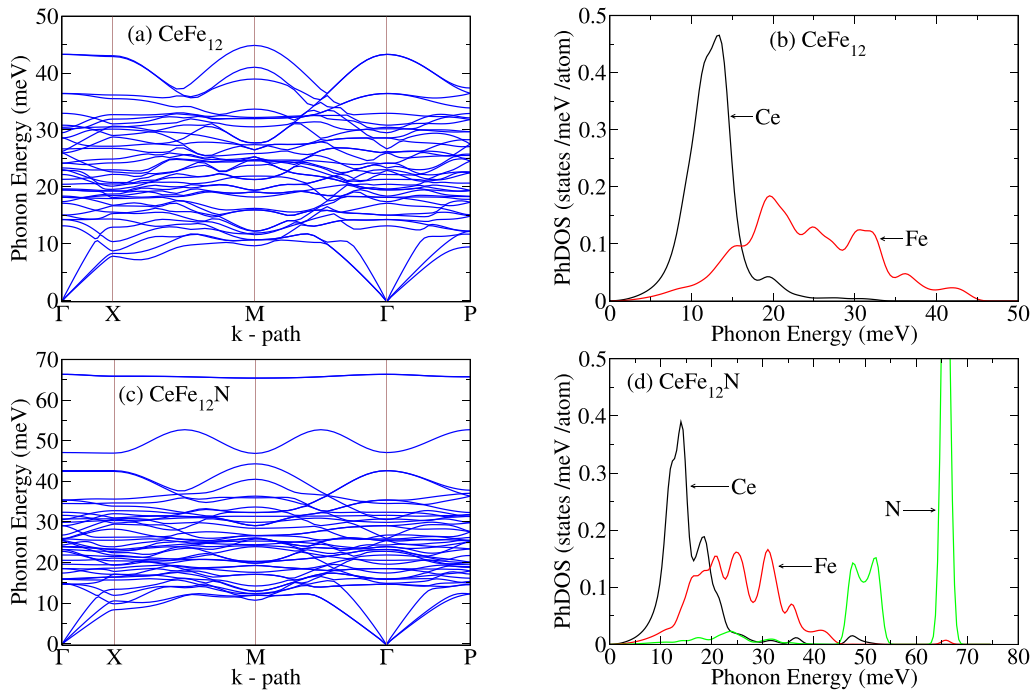


FIG. 2. Phonon band structures along the high symmetry \mathbf{k} points: $\Gamma = (0, 0, 0)$, $X = (0, 0, 1/2)$, $M = (1/2, 1/2, -1/2)$, and $P = (1/4, 1/4, 1/4)$ in units of reciprocal vectors in (a) CeFe_{12} and (c) CeFe_{12}N . The atom resolved partial phonon density of states (PhDOS) are shown in (b) CeFe_{12} and (d) CeFe_{12}N . In CeFe_{12}N , PhDOS shows the higher energy optic modes that correspond to mainly the vibrations of N. The phonon dispersions in both compounds show no soft-mode frequencies confirming their dynamical stability.

free energy in the nitrogen-added composition, specifically for $\text{CeTiFe}_{11}\text{N}$. This change is expected and can be explained by taking an average atomic mass M_{ave} . The M_{ave} decreases

with the addition of light elements. The phonon frequency increases assuming the inverse relation with $\sim M_{\text{ave}}$. It leads to an increase of the phonon frequency, which in turn enhances

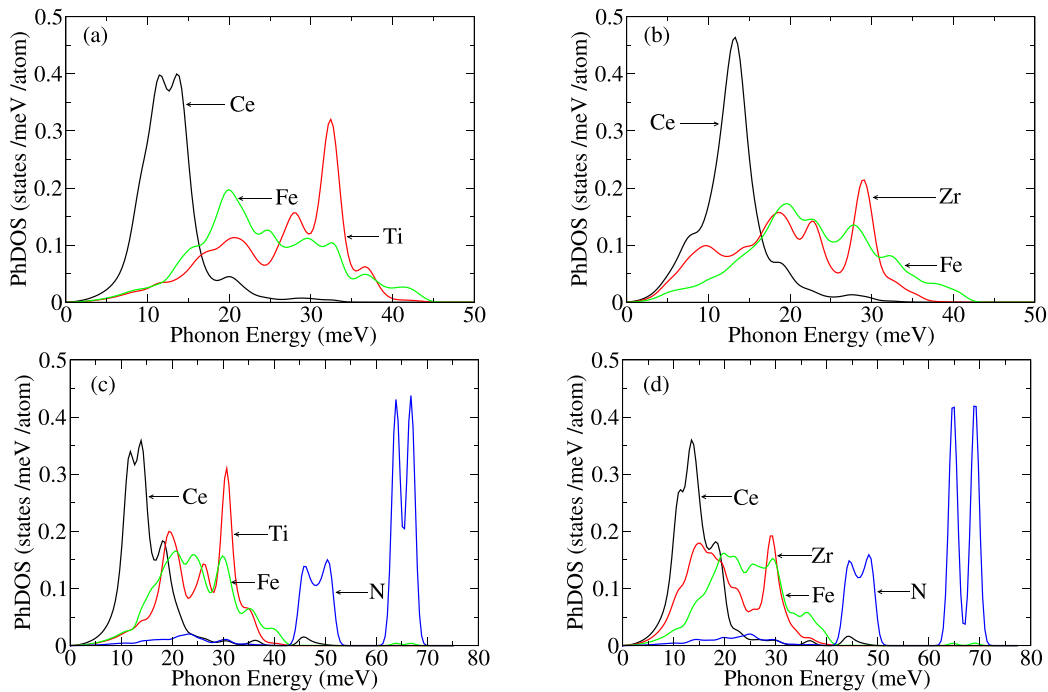


FIG. 3. Partial phonon density of states (PhDOS) of individual atoms in (a) CeTiFe_{11} , (b) CeZrFe_{11} , (c) $\text{CeTiFe}_{11}\text{N}$, and (d) $\text{CeZrFe}_{11}\text{N}$. For Fe, we show only the average value. The PhDOS show no soft-mode frequencies indicating their dynamical stability. The majority of PhDOS in low energy sector are Ce-derived as expected for heavier atoms and higher energy sector are N-derived.

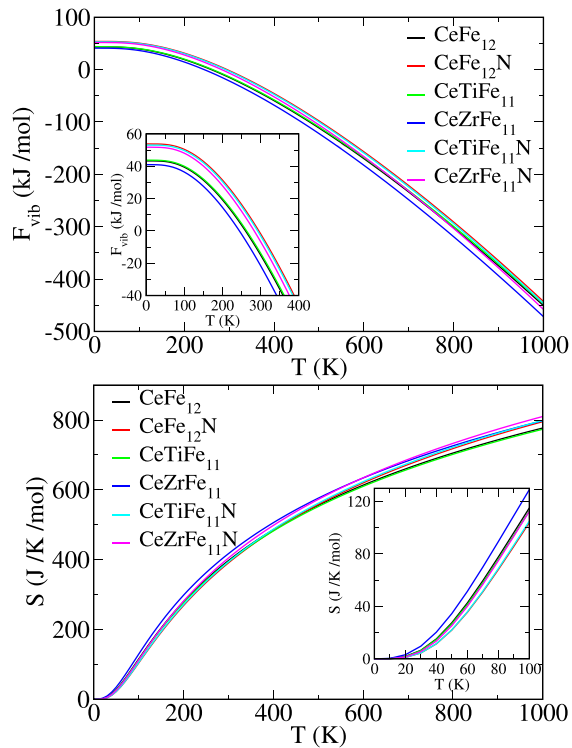


FIG. 4. Comparison of calculated vibrational Helmholtz free energy, F_{vib} , and entropy, S , in pure and site-substituted compositions. Since atomic masses of Ti and Fe are not so different, there is not much difference in the F_{vib} between CeFe_{12} and CeTiFe_{11} . Addition of nitrogen decreases the effective mass of unit cell leading to an increase of the phonon energy in CeFe_{12}N , which results in an increase of F_{vib} . The entropy changes oppositely. Insets show the enlarged view of figures.

F_{vib} . The consistent trend is also seen in the entropy (Fig. 4, bottom panel).

D. Electronic structure

Cerium is a bit tricky element as it exhibits a mixed-valence state between Ce^{3+} and Ce^{4+} depending upon the crystal environment [11,14,20]. For isolated Ce atom, the electronic configuration is $[\text{Xe}]4f^15d^16s^2$. However, in crystal, Ce $5d$ and $6s$ states lie relatively above the Fermi level, so the three valence electrons (one from $5d$ and two from $6s$) act as conduction electrons resulting in Ce^{3+} . In some cases, the remaining one $4f$ also shows a similar behavior yielding a Ce^{4+} .

In Ce^{3+} with one $4f$ electron, i.e., $4f^1$ is more localized and plays a crucial role in magnetism. In Ce^{4+} , the conduction electrons are more delocalized, and they have a negligible contribution to the intrinsic magnetic properties. Such valence fluctuation is well-known to drive a γ - α transition in Ce metal [38]. In standard pseudopotential-based DFT, one generally treats $4f$ states as core states (frozen $4f$ -core approximation) [39]. In reality, this approximation does not properly describe the physics if $4f$ states are near the Fermi level, which is also the case for Ce 1:12 compounds. We, therefore, include $4f$ states as valence states in our partial density of states (PDOS)

and MCA calculations with proper treatment of electron correlation.

The computed PDOS (by projecting the Kohn-Sham wave function inside the atomic sphere) for each element in different compositions is shown in Fig. 5. In CeFe_{12} , the Ce($4f$) states are around the Fermi level with a sudden jump (discontinuity) which presumably causes structural instability. The $4f$ peak shifts further above the Fermi level with the addition of nitrogens. The N(p) states hybridize with Ce($4f$) as well as with Fe($3d$) that enhances the crystal binding consistent with the formation energy. The Ti leads to a slight shift up of Ce($4f$) from the Fermi level, which helps to stabilize the structure. With Zr-substitution, while the $4f$ -peak shifts significantly up, the other crystal-field-split-off peak appears at the Fermi level that slightly reduces the formation energy compared to Ti. In both Ti/Zr substitutions, the Ce($4f$) features evolve in the same way with the addition of nitrogens. For example, in both cases, the formation energy as discussed earlier increases by a factor of ~ 3 , consistent with the disappearance of $4f$ peaks at the Fermi level. In addition, we note here that the three nonequivalent Fe atoms have slightly different DOS (Fig. 5). The $3d$ states of these Fe atoms hybridize slightly differently with Ti and Zr in $\text{CeFe}_{11}\text{Ti}$ and $\text{CeFe}_{11}\text{Zr}$. The $2p$ states of nitrogens also hybridize differently with these $3d$ states in $\text{CeFe}_{11}\text{TiN}$ and $\text{CeFe}_{11}\text{ZrN}$, pushing Ce $4f$ -states to a higher energy that may lead to the slightly different exchange couplings (see Ref. [22] for Ti-based systems) lowering the formation energy.

To get a more quantitative picture of the Ce-valence state, we compute the net Ce($4f$) charges which are given in Table IV by integrating the Ce-PDOS. In CeFe_{12} , we find 0.93 electrons per Ce($4f$) indicating nearly Ce^{3+} . The addition of N leads to reduction in the net $4f$ charge in CeFe_{12}N which is in contrast with $\text{CeTiFe}_{11}\text{N}$, where it remains almost the same as in CeFe_{12} . The net $4f$ charge in CeTiFe_{11} is similar to CeFe_{12}N . Interestingly, the computed net charge 0.72 e, i.e., the valency of 3.28 ($\text{Ce}^{3.28+}$) in CeTiFe_{11} is in excellent agreement with the experimental value of 3.33 ($\text{Ce}^{3.33+}$) obtained with XAFS measurement [11]. However, we do not find such differences regardless of nitrogens for Zr substitutions.

Our calculated magnetic moments for all compositions are given in Table V. For CeFe_{12} , magnetic moment is $0.45\mu_B$, which is much smaller than the expected value of $1\mu_B$ for $S = 1/2$. This indicates that the Ce is not really in $S = 1/2$ state where only one *localized* orbital is fully occupied. The Ti substitution in CeFe_{12} leads to a net decrease of the magnetic moment by $\sim 5\mu_B$ per f.u. and it is well within the range of the experimental values [4,12,16]. First, the reduction is due to the antiparallel spin moments of Ti with respect to Fe-spin moments. Second, the Fe-spin moments reduce themselves. On the other hand, the addition of nitrogen in CeFe_{12} results in a net increase of magnetic moment both in pure and Ti-substituted compositions. The increases of net magnetic moment in $\text{CeTiFe}_{11}\text{N}$ is consistent with the experiments by $\sim 2\mu_B$ per f.u. [13,16]. Nitrogen reduces the Ce (by almost a factor of 4) and Fe($8i$) spin moments. On the other hand, it enhances the Fe($8f$) and Fe($8j$) spin moments. Interestingly, we find Ce close to Ce^{3+} in $\text{CeTiFe}_{11}\text{N}$, CeZrFe_{11} , and $\text{CeZrFe}_{11}\text{N}$, although Ce is not really in $S = 1/2$ state. A similar trend is also found in the Zr-substituted compositions,

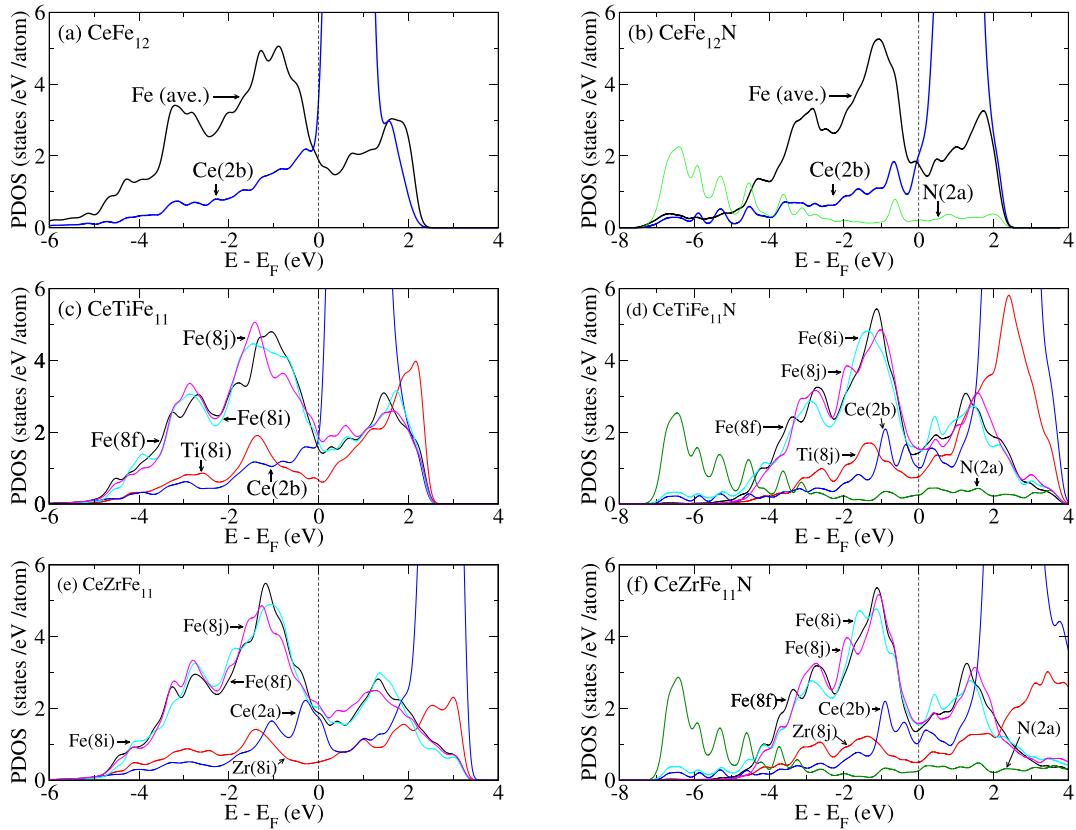


FIG. 5. Partial density of states (PDOS) of individual atoms in (a) CeFe_{12} , (b) CeFe_{12}N , (c) CeTiFe_{11} (d) $\text{CeTiFe}_{11}\text{N}$, (e) CeZrFe_{11} , and (f) $\text{CeZrFe}_{11}\text{N}$ obtained with GGA + U + SOC calculations. In CeFe_{12} and CeFe_{12}N , we show average PDOS for Fe atoms. In CeTiFe_{11} , Ce(4*f*) peak lies above the Fermi level without a clear splitting. In other cases, PDOS show split-off 4*f* states around the Fermi level.

except now Ce exhibits a $S \sim 1/2$ state in CeZrFe_{11} . The net magnetic moment is larger in Zr, which is partly due to the reduced value of Zr-spin moments in CeZrFe_{11} . It is expected for Zr as the Zr(4*d*) orbitals are more delocalized than Ti(3*d*) orbitals. Indeed, the bandwidth of Zr(4*d*) orbital is larger by ~ 1 eV than Ti(3*d*) as can be seen in Fig. 5.

Qualitatively, the spin moment of Ce can be explained by analyzing spin-density contours. The computed spin-density contours are shown in Fig. 6 for three representative cases. We note that the mixings among Ce 6*s*, 5*d*, and 4*f* states around the Fermi level are negligible, so the net spin-density contours shown here mainly represent the Ce(4*f*) spin moments. For CeFe_{12} , the contour [Fig. 6(a)] is strongly polarized along the

crystalline *c* direction although, the spin moment is significantly reduced. We find substantial changes in the contour with N and Ti or Zr substitutions (not all shown here) that reflect the variation of Ce(4*f*) spin moment. For instance, the contour [Fig. 6(b)] is perturbed significantly with the addition of nitrogens, which is consistent with the reduced spin moment of Ce in CeFe_{12}N . It further suggests that the nitrogen-added itinerant electrons drastically modify the spin polarization, which ultimately affects the spin moment of Ce(4*f*). The sign of spin-moment is also reversed in Ti- or Zr-substituted compositions by nitrogens. While both Ti- and Zr-substitutions perturb the spin density, the net Ce(4*f*) spin moment is much larger in later [Fig. 6(c)].

TABLE IV. Total amount of electrons (in units of *e*) occupying Ce(4*f*) state and spin magnetic moment (μ_s) and orbital magnetic moment (μ_l) in units of μ_B in pure and site-substituted compounds. The values of μ_l outside and inside the parenthesis correspond to obtained along the [001] and [100] directions. For $\text{CeZrFe}_{11}\text{N}$, μ_l is also provided for the [010] direction in which lattice constant mismatch is the largest. The net electron occupying Ce(4*f*) is ~ 1 *e* in all compounds except CeFe_{12}N and CeTiFe_{11} , showing the formation of Ce^{3+} . The spin-moment of Ce(4*f*) is far from ideal value $1\mu_B$ for $S = 1/2$ except for CeZrFe_{11} .

	CeFe_{12}	CeFe_{12}N	$\text{CeTiFe}_{11}\text{N}$	CeTiFe_{11}	$\text{CeZrFe}_{11}\text{N}$	CeZrFe_{11}
electron	0.93	0.74	0.91	0.72	0.92	0.94
μ_s	-0.45	-0.1	0.58	-0.38	0.61	-0.78
μ_l	0.42(0.26)	0.16(-0.02)	0.05(-0.47)	0.24(0.2)	0.04(-0.51 ^a , -0.49 ^b)	0.60(-0.02)

^aAlong [100].

^bAlong [010].

TABLE V. The total magnetic moment of each atom and the total magnetic moment per f.u. (including the interstitial contributions for spin moments). Experimental data (the net magnetic moment) are available only for Ti-substituted compositions. The net magnetic moment of cerium is negative for all except in CeTiFe₁₁N and CeZrFe₁₁N, which helps partly in enhancing the net magnetic moment.

Atom	CeFe ₁₂	CeFe ₁₂ N	CeTiFe ₁₁ N	CeTiFe ₁₁	CeZrFe ₁₁ N	CeZrFe ₁₁
Ce(2a/2b)	−0.56	−0.13	0.44	−0.42	0.46	−0.46
Fe(8f)	1.91	2.33	2.26	1.81	2.31	1.98
Fe(8i)	2.55	2.14	2.08	2.31	2.06	2.06
Fe(8j)	2.36	2.63	2.43	2.19	2.46	2.25
Ti/Zr(8i)			−0.81	−0.75	−0.50	−0.47
N(2a)		0.03	−0.01		−0.02	
Total	26.36	28.09	24.06	21.58	25.13	22.72
Expt. [4,12,16]				17.4–20.2		

E. Magnetic anisotropy

Rare-earth-based 1:12 compounds exhibit rather subtle magnetic anisotropy behavior with addition of nitrogen atoms in the interstitial sites [13,16,41]. For example, NdFe₁₂N and NdTiFe₁₁N show an increase in the MCA [41], while in CeTiFe₁₁N it is the opposite [13]. In Ref. [24], authors report easy-plane MCA for CeFe₁₂ using dynamical mean-field theory (quantum Monte Carlo) calculations disagreeing with

DFT results. They predicted a larger value in CeTiFe₁₁N than in CeTiFe₁₁ contrary to the experiment, which may be the artifact of too-simplified assumption, $J = 5/2$ state for Ce.

To predict MCA, we perform self-consistent total energy calculations along the [001] and [100] crystalline directions. Then the magnetic anisotropy constant is obtained as $K_1 = \{E[100] - E[001]\}/V$, where V is the volume of the unit cell, with GGA and GGA + U methods including SOC as given in Table VI. We note that the values of K_1 obtained with respect to b axis, i.e., $K_1 = \{E[010] - E[001]\}/V$ are very similar to that with respect to a axis, except for nitrides. Especially, the largest difference (0.2 MJ/m³) is predicted for CeZrFe₁₁N for which the lattice constant mismatch is the largest in the ab plane. The values of K_1 follow the trends of orbital magnetic moment, i.e., larger the orbital moment difference between easy and hard axes provided they have the same sign, larger the value of K_1 . Further, we checked the convergence of MCA in CeFe₁₂N by using the dense \mathbf{k} mesh up to $8 \times 8 \times 14$ and found no significant changes (an increase by 0.1 MJ/m³). Both methods predict K_1 positive confirming all of them uniaxial along the crystalline c direction, i.e., c axis as an easy axis and a or b as a hard axis, while magnitudes differ. The GGA + SOC yields much smaller values for CeFe₁₂, CeFe₁₂N, and CeZrFe₁₁ than GGA + U + SOC. For CeTiFe₁₁, the measured value of K_1 is in the range 0.76–4.3 MJ/m³ [4,12,13,16,40], which agrees with our prediction. Since these experiments utilize different synthesis procedures, purity of constituent elements, and heat treatment with different starting compositions with and without interstitial elements, it is reasonable to find different values of K_1 in CeTiFe₁₁. All previous theory calculations yielded much smaller values except in the Ref. [21]. Our results show that the inclusion of the on-site electron correlation effect improves K_1 forming a split-off $4f$ states at the Fermi level as discussed above (Fig. 5). Overall, nitrogens reduce the magnitude of K_1 .

The MCA of 1:12 compounds is primarily governed by the $4f$ electrons of rare earth, which is also true for CeFe₁₂. To illustrate this, we show the contours for Ce spin density (Fig. 6), which is the charge occupying the Ce($4f$) states in CeFe₁₂ and CeZrFe₁₁. Specifically, for CeFe₁₂, as stated earlier, it is the $4f$ orbital along the anisotropic axis that requires a huge amount of magnetic energy to rotate it away from the crystalline c axis even if the orbital moment is small (orbital moment is $\sim 0.4\mu_B$ for Ce). It is somewhat

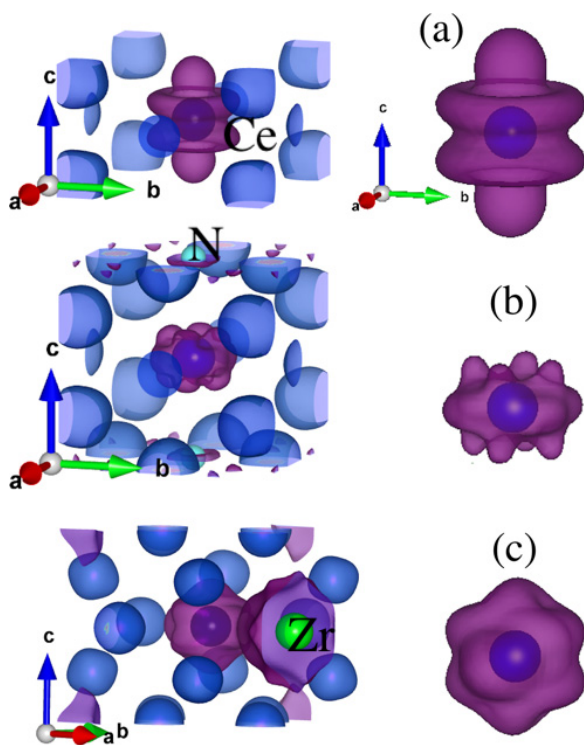


FIG. 6. Electron spin density contours of Ce and nearby atoms (left) and enlarged view of Ce-only (right) where contours in blue are spin- \uparrow and purple are spin- \downarrow electrons. Spin- \uparrow corresponds to net electron occupying Ce($4f$) states (isosurface $0.006 e/\text{\AA}^3$) in (a) CeFe₁₂, (b) CeFe₁₂N, and (c) CeZrFe₁₁. Contour (a) corresponds to an admixture of $4f$ states with strongly quenched orbital moment. The shape of the contour is drastically modified by itinerant electrons of nitrogens in CeFe₁₂N (b), which reduces the magnetic anisotropy. On the other hand, Zr enhances the magnetic anisotropy by perturbing the contour (c) in CeZrFe₁₁.

TABLE VI. Calculated magnetic anisotropy constant K_1 and its comparison with experiment and literature. The values inside and outside the parenthesis (in units of MJ/m³) are obtained with GGA+SOC and GGA + U + SOC. While both methods yield positive value of K_1 , GGA + U + SOC produces the largest value for CeZrFe₁₁.

K_1	CeFe ₁₂	CeFe ₁₂ N	CeTiFe ₁₁ N	CeTiFe ₁₁	CeZrFe ₁₁ N	CeZrFe ₁₁
This work	4.7(0.65)	2.44(0.87)	3.2(2.42)	3.29(2.35)	3.42(2.55)	7.36(1.98)
Expt. [4,12,13,16,40]				0.76–4.3		
Theory			1.62 ^a	1.57 ^b , 1.98 ^a , 11 ^c		

^aDFT LMTO [22].

^bDFT plane wave [23].

^cDFT ASA [21].

similar to that observed in the lanthanum hexaferrite where $3dz^2$ -state contributes to MCA [42]. Nitrogens lead to a much-reduced size of the spin-density contour [Fig. 6(b)] that is consistent with reduced value of magnetic moment for Ce in CeFe₁₂N. The net charge distribution presumably distorts significantly, which leads to a reduction of K_1 in CeFe₁₂N. With Zr substitution, the charge polarization around Ce is also expected to change [Fig. 6(c)], as Zr spin moments are parallel to Ce-moments, unlike Fe-spin moments which are antiparallel to Ce-spin moments. The magnitude of K_1 in GGA + U + SOC, is the largest for CeZrFe₁₁ for two reasons. First, effectively, the spin density is uniaxial. Second, Ce displays Ce³⁺-state with $S \sim 1/2$, and $L = 0.6$ (Table IV) in CeZrFe₁₁ that results in a stronger SOC than in CeTiFe₁₁.

IV. SUMMARY

By performing the first-principles electronic structure calculations, we investigate the lattice stability and the intrinsic magnetic properties of Ti- or Zr-substituted Ce-based 1:12 materials. The formation energies indicate that all the compositions can form in the bulk structure except CeFe₁₂. We compute the phonon dispersions for Ti/Zr-substituted rare-earth-based (Ce 1:12) intermetallic compounds. We find no soft-mode frequencies that indicate all compositions are dynamically stable. The mixed valency of Ce is confirmed by examining the electronic structure in different approxi-

mations, e.g., with Ce(4*f*) as core- and valence- electrons, including the on-site electron-correlation effect. The computed Ce(4*f*) charges suggest that the valence state fluctuates between Ce³⁺ and Ce⁴⁺ depending upon the substituted element as well as the nitrogens. Interestingly, the net magnetic moment is predicted larger in Zr substitution than in Ti substitution, which is attributed to a more delocalized nature of Zr(4*d*) orbitals. The interstitial nitrogens improve the net magnetic moment for all consistent with experiments. The on-site electron correlation is crucial for the MCA due to the mixed-valence character of Ce. The predicted values of K_1 show all compositions uniaxial along the crystalline c direction. Specifically, the value of K_1 is the largest for CeZrFe₁₁ caused by the polarization of Ce(4*f*) charge along the c axis and stronger SOC, which would be interesting to examine experimentally.

ACKNOWLEDGMENTS

This work is supported by the Critical Materials Institute, an Energy Innovation Hub funded by the U.S. Department of Energy, Office of Energy Efficiency and Renewable Energy, Advanced Manufacturing Office. The Ames Laboratory is operated for the U.S. Department of Energy by Iowa State University of Science and Technology under Contract No. DE-AC02-07CH11358. We would like to acknowledge Ed Moxley for maintaining and updating computational facilities and software.

- [1] J. M. D. Coey, Hard magnetic materials: A perspective, *IEEE Trans. Magn.* **47**, 4671 (2011).
- [2] Y. Harashima, K. Terakura, H. Kino, S. Ishibashi, and T. Miyake, Nitrogen as the best interstitial dopant among X = B, C, N, O, and F for strong permanent magnet NdFe₁₁TiX: First-principles study, *Phys. Rev. B* **92**, 184426 (2015).
- [3] T. Yoshioka, H. Tsuchiura, and P. Novák, Statistical and analytical approaches to finite-temperature magnetic properties of the compound SmFe₁₂, *Phys. Rev. B* **102**, 184410 (2020).
- [4] C. Zhou, F. E. Pinkerton, and J. F. Herbst, Magnetic properties of CeFe_{11-x}Co_xTi with ThMn₁₂ structure, *J. Appl. Phys.* **115**, 17C716 (2014).
- [5] I. S. Tereshina, N. V. Kostyuchenko, E. A. Tereshina-Chitrova, Y. Skourski, M. Doerr, I. A. Pelevin, A. K. Zvezdin, M. Paukov, L. Havela, and H. Drulis, ThMn₁₂-type phases for magnets with low rare-earth content: Crystal-field analysis of the full magnetization process, *Sci. Rep.* **8**, 3595 (2018).
- [6] G. Hadjipanayis, A. Gabay, A. Schönhöbel, A. Martín-Cid, J. Barandiaran, and D. Niarchos, ThMn₁₂-type alloys for permanent magnets, *Engineering* **6**, 141 (2020).
- [7] A. Makurenkova, D. Ogawa, P. Tozman, S. Okamoto, S. Nikitin, S. Hirotsawa, K. Hono, and Y. Takahashi, Intrinsic hard magnetic properties of Sm(Fe,Co)_{12-x}Ti_x compound with ThMn₁₂ structure, *J. Alloys Compd.* **861**, 158477 (2021).
- [8] Y. Hirayama, T. Miyake, and K. Hono, Rare-earth lean hard magnet compound NdFe₁₂N, *JOM* **67**, 1344 (2015).
- [9] M. Bacmann, C. Baudelet, D. Fruchart, D. Gignoux, E. Hlil, G. Krill, M. Morales, R. Vert, and P. Wolfers, Exchange interactions and magneto-crystalline anisotropy in RFe_{12-x}M_x and parent interstitial compounds, *J. Alloys Compd.* **383**, 166 (2004).
- [10] J. Zhang, X. Tang, H. Sepelri-Amin, A. Srinithi, T. Ohkubo, and K. Hono, Origin of coercivity in an anisotropic

- Sm(Fe,Ti,V)₁₂-based sintered magnet, *Acta Mater.* **217**, 117161 (2021).
- [11] O. Isnard, S. Miraglia, and F. Villain, XAFS study of the Ce valence in magnetic Ce intermetallic compounds, *J. Phys. IV (France)* **7**, C2 (1997).
- [12] O. Isnard, S. Miraglia, M. Guillot, and D. Fruchart, Hydrogen effects on the magnetic properties of RFe₁₁Ti compounds, *J. Alloys Compd.* **275-277**, 637 (1998).
- [13] M. Akayama, H. Fujii, K. Yamamoto, and K. Tatami, Physical properties of nitrogenated RFe₁₁Ti intermetallic compounds (R=Ce, Pr and Nd) with ThMn₁₂-type structure, *J. Magn. Mater.* **130**, 99 (1994).
- [14] E. Shoko, M. F. Smith, and R. H. McKenzie, Mixed valency in cerium oxide crystallographic phases: Valence of different cerium sites by the bond valence method, *Phys. Rev. B* **79**, 134108 (2009).
- [15] Y. Harashima, T. Fukazawa, and T. Miyake, Cerium as a possible stabilizer of ThMn₁₂-type iron-based compounds: A first-principles study, *Scr. Mater.* **179**, 12 (2020).
- [16] Q. Pan, Z. Liu, and Y. Yang, Structural and magnetic properties of Ce(Fe,M)₁₂N_x interstitial compounds, M=Ti, V, Cr, and Mo, *J. Appl. Phys.* **76**, 6728 (1994).
- [17] Y. Yang, X. Zhang, S. Ge, Q. Pan, L. Kong, H. Li, J. Yang, B. Zhang, Y. Ding, and C. Ye, Magnetic and crystallographic properties of novel Fe-rich rare-earth nitrides of the type RTiFe₁₁N₁₋₈ (invited), *J. Appl. Phys.* **70**, 6001 (1991).
- [18] J. Coey, H. Sun, and D. Hurlley, Intrinsic magnetic properties of new rare-earth iron intermetallic series, *J. Magn. Mater.* **101**, 310 (1991).
- [19] J. M. D. Coey, J. E. M. Allan, A. A. Minakov, and Y. V. Bugaslavsky, Ce₂Fe₁₇: Mixed valence or 4f band?, *J. Appl. Phys.* **73**, 5430 (1993).
- [20] O. Eriksson, L. Nordström, M. S. S. Brooks, and B. Johansson, 4f-Band Magnetism in CeFe₂, *Phys. Rev. Lett.* **60**, 2523 (1988).
- [21] W. Körner, G. Krugel, and C. Elsässer, Theoretical screening of intermetallic ThMn₁₂-type phases for new hard-magnetic compounds with low rare earth content, *Sci. Rep.* **6**, 24686 (2016).
- [22] L. Ke and D. D. Johnson, Intrinsic magnetic properties in R(Fe_{1-x}Co_x)₁₁TiZ (R = Y and Ce; Z = H, C, and N), *Phys. Rev. B* **94**, 024423 (2016).
- [23] R. Martinez-Casado, A. Dasmahapatra, M. F. Sgroi, C. Romero-Muñiz, H. C. Herper, O. Y. Vekilova, A. M. Ferrari, D. Pullini, J. Desmarais, and L. Maschio, The CeFe₁₁Ti permanent magnet: a closer look at the microstructure of the compound, *J. Phys.: Condens. Matter* **31**, 505505 (2019).
- [24] A. Galler, S. Ener, F. Maccari, I. Dirba, K. P. Skokov, O. Gutfleisch, S. Biermann, and L. V. Pourovskii, Intrinsically weak magnetic anisotropy of cerium in potential hard-magnetic intermetallics, *npj Quantum Mater.* **6**, 2 (2021).
- [25] G. Kresse and J. Hafner, *Ab initio* molecular dynamics for liquid metals, *Phys. Rev. B* **47**, 558 (1993).
- [26] G. Kresse and D. Joubert, From ultrasoft pseudopotentials to the projector augmented-wave method, *Phys. Rev. B* **59**, 1758 (1999).
- [27] J. P. Perdew, K. Burke, and Y. Wang, Generalized gradient approximation for the exchange-correlation hole of a many-electron system, *Phys. Rev. B* **54**, 16533 (1996).
- [28] J. Paier, R. Hirschl, M. Marsman, and G. Kresse, The Perdew-Burke-Ernzerhof exchange-correlation functional applied to the G2-1 test set using a plane-wave basis set, *J. Chem. Phys.* **122**, 234102 (2005).
- [29] S. L. Dudarev, G. A. Botton, S. Y. Savrasov, C. J. Humphreys, and A. P. Sutton, Electron-energy-loss spectra and the structural stability of nickel oxide: An LSDA+U study, *Phys. Rev. B* **57**, 1505 (1998).
- [30] I. L. M. Locht, Y. O. Kvashnin, D. C. M. Rodrigues, M. Pereira, A. Bergman, L. Bergqvist, A. I. Lichtenstein, M. I. Katsnelson, A. Delin, A. B. Klautau, B. Johansson, I. Di Marco, and O. Eriksson, Standard model of the rare earths analyzed from the Hubbard *i* approximation, *Phys. Rev. B* **94**, 085137 (2016).
- [31] S. Baroni, S. de Gironcoli, A. Dal Corso, and P. Giannozzi, Phonons and related crystal properties from density-functional perturbation theory, *Rev. Mod. Phys.* **73**, 515 (2001).
- [32] C. L. Fu, A. J. Freeman, E. Wimmer, and M. Weinert, Frozen-Phonon Total-Energy Determination of Structural Surface Phase Transitions: W(001), *Phys. Rev. Lett.* **54**, 2261 (1985).
- [33] G. Xing, T. Ishikawa, Y. Miura, T. Miyake, and T. Tadano, Lattice dynamics effects on finite-temperature stability of R_{1-x}Fe_x (R = Y, Ce, Nd, Sm, and Dy) alloys from first principles, *J. Alloys Compd.* **874**, 159754 (2021).
- [34] H. I. Sözen, S. Ener, F. Maccari, K. P. Skokov, O. Gutfleisch, F. Körmann, J. Neugebauer, and T. Hickel, *Ab initio* phase stabilities of Ce-based hard magnetic materials and comparison with experimental phase diagrams, *Phys. Rev. Materials* **3**, 084407 (2019).
- [35] P. Tozman, H. Sepehri-Amin, Y. Takahashi, S. Hirosawa, and K. Hono, Intrinsic magnetic properties of Sm(Fe_{1-x}Co_x)₁₁Ti and Zr-substituted Sm_{1-y}Zr_y(Fe_{0.8}Co_{0.2})_{11.5}Ti_{0.5} compounds with ThMn₁₂ structure toward the development of permanent magnets, *Acta Mater.* **153**, 354 (2018).
- [36] M. Matsumoto, T. Hawaii, and K. Ono, (Sm, Zr)Fe_{12-x}M_x (M = Zr, Ti, Co) for permanent-magnet applications: *Ab initio* material design integrated with experimental characterization, *Phys. Rev. Applied* **13**, 064028 (2020).
- [37] A. Togo and I. Tanaka, First principles phonon calculations in materials science, *Scr. Mater.* **108**, 1 (2015).
- [38] B. Johansson, The $\alpha - \gamma$ transition in cerium is a mott transition, *Philos. Mag.* **30**, 469 (1974).
- [39] M. Dolg, H. Stoll, A. Savin, and H. Preuss, Energy-adjusted pseudopotentials for the rare earth elements, *Theor. Chim. Acta* **75**, 173 (1989).
- [40] D. Goll, R. Loeffler, R. Stein, U. Pflanz, S. Goeb, R. Karimi, and G. Schneider, Temperature dependent magnetic properties and application potential of intermetallic Fe_{11-x}Co_xTiCe, *Phys. Status Solidi RRL* **8**, 862 (2014).
- [41] Y. Hirayama, Y. Takahashi, S. Hirosawa, and K. Hono, NdFe₁₂N_x hard-magnetic compound with high magnetization and anisotropy field, *Scr. Mater.* **95**, 70 (2015).
- [42] C. Bhandari, M. E. Flatté, and D. Paudyal, Enhanced magnetic anisotropy in lanthanum M-type hexaferrites by quantum-confined charge transfer, *Phys. Rev. Materials* **5**, 094415 (2021).